

Separation-free artificial photosynthesis of concentrated hydrogen peroxide and value-added fuels over Ta atomic sites

Received: 10 March 2025

Accepted: 1 September 2025

Published online: 02 October 2025

Check for updates

Hao Tan^{1,2,6}, Peng Zhou^{3,6}, Yu Gu¹, Youxing Liu¹, Wenxing Chen⁴, Hongyu Guo¹, Fangxu Lin¹, Heng Luo¹, Xiaoqing Cao¹, Lingyou Zeng¹, Mingchuan Luo^{1,5} & Shaojun Guo^{1,5}✉

Solar-driven artificial photosynthesis of hydrogen peroxide and high-value chemicals from oxygen and biomass is promising but is hindered by poor light absorption, sluggish kinetics of biomass dehydrogenation, and low oxygen reduction selectivity. Herein, we develop a resorcinol-formaldehyde resin/carbon-supported Ta-N₂O₂ single-atom catalyst (RF/C-TaSA) that enables broad-spectrum light harvesting (> 932 nm) and selective biomass conversion in a solid-organic-aqueous three-phase system. RF/C-TaSA achieves a high 3.0% quantum yield at 635 nm, with Ta-N₂O₂ sites stabilizing intermediates and reducing the energy barrier for biomass conversion. We further demonstrate that RF/C-TaSA enables efficient artificial photosynthesis of H₂O₂ and value-added chemicals from more available thatch, pine needles and wastepaper. Combining catalyst innovation and system engineering, we build a solar-powered RF/C-TaSA-based photocatalytic device for directly producing commercially viable H₂O₂ at a high concentration of 3 wt% and high-value-added chemical without requiring energy-intensive separation processes for 70-day operation. Furthermore, the produced crude concentrated H₂O₂ can also be readily converted to solid H₂O₂ powder (Na₂CO₃ • 1.5 H₂O₂) for ease of storage and transport with high sterilization activities even after 6 months.

Hydrogen peroxide (H₂O₂) is an indispensable feedstock in industries with a global demand reaching ~5.7 million tons by 2027¹. Powered by renewable solar energy, artificial photosynthesis of H₂O₂ is a highly desirable strategy compared to the current energy-consuming and waste-intensive industrial anthraquinone method². Although recent reported photocatalysts like carbon nitride and covalent organic frameworks, have been reported to facilitate the direct photosynthesis of H₂O₂ through either a two-electron or four-electron water oxidation reaction pathway, accompanied by a concomitant two-electron

oxygen reduction reaction²⁻⁴, they show quite limited performance (low-concentration H₂O₂ production (<0.5 mM)) in the photosynthesis of hydrogen peroxide due to their sluggish water oxidation reaction (WOR), low light absorption property and undesirable decomposition of H₂O₂ product⁴⁻⁶. Though the use of sacrificial agents (e.g. triethanolamine⁷, ethanol⁸, etc.) during the photocatalytic process enabled an increased concentration of H₂O₂, the sacrificial chemicals are often over-oxidized to carbon oxide (CO or CO₂) or other wastes⁹. Steering the oxidation of sacrificial agents towards value-added

¹School of Materials Science and Engineering, Peking University, Beijing, PR China. ²Shenyang National Laboratory for Materials Science, Institute of Metal Research, Chinese Academy of Sciences, Shen-yang, PR China. ³School of Environment and Energy, Peking University Shenzhen Graduate School, Shenzhen, Guangdong, PR China. ⁴Energy & Catalysis Center, School of Materials Science and Engineering, Beijing Institute of Technology, Beijing, China. ⁵The Beijing Innovation Center for Engineering Science and Advanced Technology, Peking University, Beijing, PR China. ⁶These authors contributed equally: Hao Tan, Peng Zhou. ✉e-mail: guosj@pku.edu.cn

chemicals can improve the economic outcome¹⁰. Despite these recent progresses, there remains a lack of suitable photocatalytic sites to lower the reactive energy barrier of dehydrogenation reaction and meanwhile inhibit the severe H₂O₂ decomposition. Furthermore, the energy-intense separation of as-produced H₂O₂ and chemicals in the reported systems represents another grand technical challenge towards photosynthetic industrialization.

To address the aforementioned challenges, we herein design a class of RF/C-TaSA composite photocatalysts with high-density Ta-N₂O₂ (abbreviated as TaSA) atomic sites anchored on carbon matrix (C-TaSA) coupled with resorcinol-formaldehyde resins (RF) (Fig. 1a and Supplementary Fig. 1). Notably, the d⁰-configuration elements of tantalum (Ta⁵⁺) can prevent intermediate band formation in the band structure, enabling broad and dispersed conduction bands, and thereby enhancing charge separation efficiency^{11,12}. By further coupling with a well-engineered solid-organic-aqueous three-phase system, herein we achieve the separation-free artificial photosynthesis of H₂O₂ and value-added chemicals under natural light irradiation. Solid-state ¹³C nuclear magnetic resonance (NMR), Fourier Transform Infrared (FTIR) and diffuse reflectance UV-vis spectra revealed that RF/C-TaSA had an optimal benzenoid-quinoid donor-acceptor (D-A) ratio, resulting in a small highest occupied molecular orbital-lowest unoccupied molecular orbital (HOMO-LUMO) gaps¹³. The small gaps endow the

RF/C-TaSA photocatalyst with a competitive apparent quantum yield of 3.0% under red light (635 nm) irradiation by harvesting the most visible light. The hydrophobic RF/C-TaSA dispersed in the organic phase shows higher mass transfer efficiency over RF, reducing the decomposition of the produced H₂O₂ in the aqueous phase. Density functional theory (DFT) simulations and experimental results reveal that the TaSA site is the active site for the dehydrogenation of biomass derivatives via a concurrent two-electron biomass dehydrogenation reaction pathway. Combining catalyst innovation and system engineering, we demonstrate that the RF/C-TaSA-based solar-powered device can prepare H₂O₂ aqueous solution with a high concentration (3 wt%) without additional separation operation in the 70-day H₂O₂ photosynthesis, which is more energy-efficient and environmentally friendly compared to traditional anthraquinone synthetic method (Supplementary Fig. 2). In addition, RF/C-TaSA photocatalyst is quite general for efficiently producing H₂O₂ from more available thatch, pine needles, and wastepaper.

Results

Synthesis and structure characterization

The composite photocatalyst (RF/C-TaSA) was prepared by fixing TaSA-loaded carbon matrix (C-TaSA) onto resorcinol-formaldehyde (RF) resins with a yolk-shell structure (Fig. 1a). The scanning electron

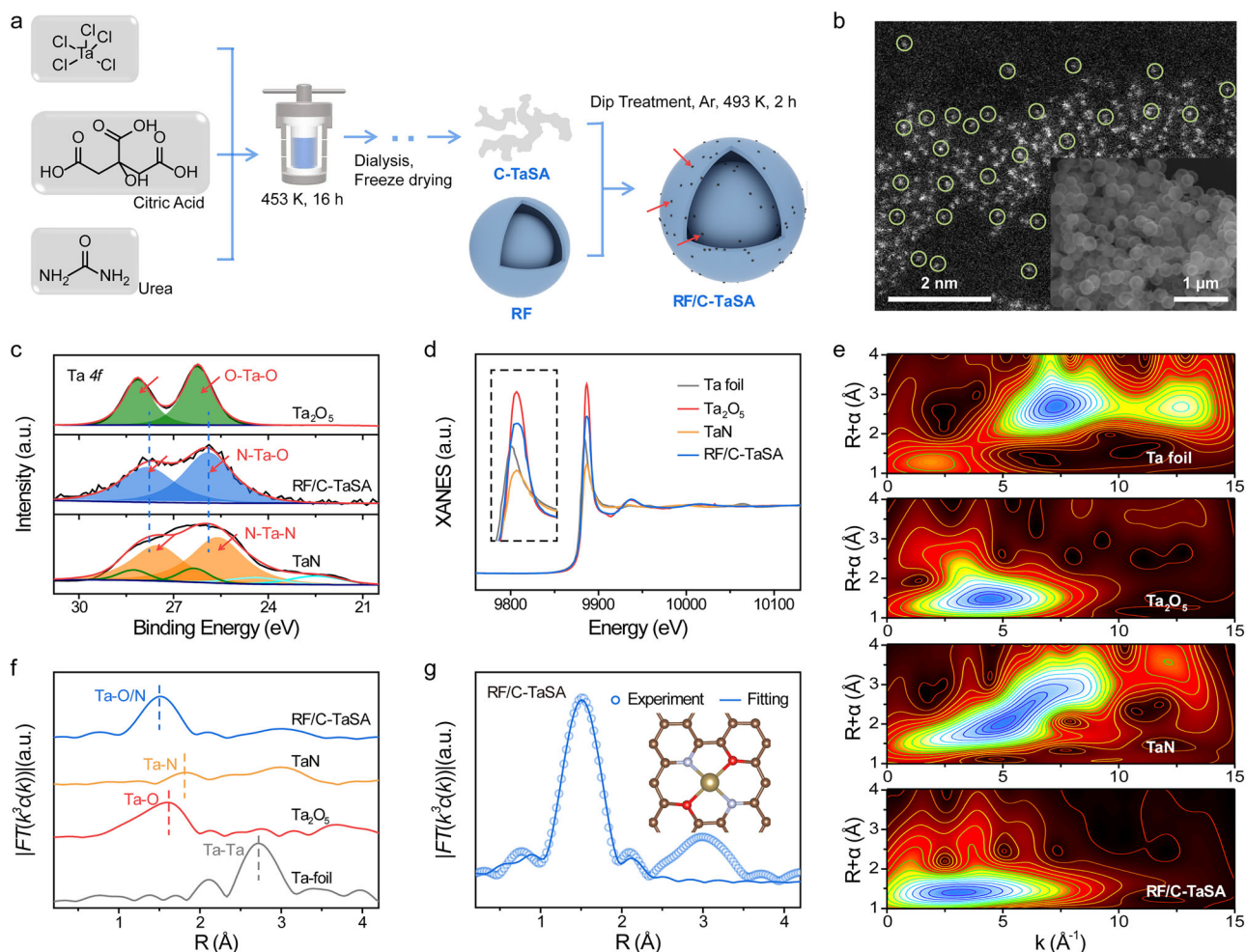


Fig. 1 | Characterizations of RF/C-TaSA. a Synthetic route of RF/C-TaSA. **b** HAADF-STEM and SEM (*inset*) images of C-TaSA and RF/C-TaSA. **c** High-resolution XPS spectra of Ta 4*f* for Ta₂O₅, TaN and RF/C-TaSA. **d** XANES of Ta foil, Ta₂O₅, TaN and RF/C-TaSA at tantalum L₃-edge. **e** Wavelet transformation for the tantalum L₃-edge XAFS signals of Ta foil, Ta₂O₅, TaN and RF/C-TaSA based on

Morlet wavelets with optimum resolution at the first and higher coordination shells. Intensity increases in the order of red, yellow, green and blue. **f** Fourier-transformed (FT) *k*³-weighted R-space EXAFS spectra of Ta foil, Ta₂O₅, TaN and RF/C-TaSA, and **g** fitting result of RF/C-TaSA. Source data are provided as a Source Data file.

microscopy (SEM) (Fig. 1b, inset) and transmission electron microscopy (TEM) images (Supplementary Fig. 3) show a yolk-shell structure of RF/C-TaSA, with an average diameter of 200 nm for yolk and a shell thickness of 30 nm. High-angle annular dark field scanning transmission electron microscopy (HAADF-STEM) image shows that Ta atoms are uniformly dispersed on the carbon matrix (Fig. 1b and Supplementary Fig. 4). X-ray photoelectron spectroscopy (XPS) and HAADF-STEM-elemental mapping of RF/C-TaSA suggest that TaSA is uniformly anchored on the RF (Supplementary Figs. 5–6). Energy-dispersive X-ray spectroscopy (EDS) result reveal that C-TaSA has a Ta content of 9.7 wt% (Supplementary Fig. 7).

The electronic property and coordinative environment of Ta were investigated by X-ray photoelectron spectroscopy (XPS) and X-ray absorption fine structure (XAS) of Ta L_{3} -edge spectra. The high-resolution Ta 4f spectrum of RF/C-TaSA suggests the formation of N-Ta-O bonding, different from O-Ta-O in Ta₂O₅ or N-Ta-N in TaN (Fig. 1c). Both absorption threshold and white line of RF/C-TaSA in X-ray absorption near-edge structure (XANES) are higher than those of Ta foil and TaN, but lower than those of Ta₂O₅, indicating that the oxidation state of Ta is close to +4 (Fig. 1d). The k^3 -weighted R-space Fourier transform spectra of RF/C-TaSA from X-ray absorption fine structure (EXAFS) demonstrate the formation of Ta-O (1.95 Å) and Ta-N (1.92 Å) coordination (Fig. 1f, g and Supplementary Fig. 8)¹⁴. Moreover, the model-based EXAFS fitting of RF/C-TaSA suggests that the Ta center with a total coordination number of 4 is coordinated with two oxygen and two nitrogen atoms (Supplementary Table 1). The wavelet transformation of Ta L_{3} -edge EXAFS results further verifies that Ta-Ta bonds are not present in RF/C-TaSA, and the peak of RF/C-TaSA tends to have a different k value than that of Ta-O in Ta₂O₅ and Ta-N in TaN, indicating that the N-Ta-O complex coordination exists in RF/C-TaSA (Fig. 1e).

The chemical configurations of different photocatalysts were investigated by Fourier Transform Infrared (FTIR) and solid-state ¹³C nuclear magnetic resonance (NMR) spectra. RF/C-TaSA exhibits a remarkably higher quinone C=O peak at 1650 cm⁻¹ in FTIR (Supplementary Fig. 9) and 183 ppm in ¹³C NMR spectra (Supplementary

Fig. 10) than bare RF, indicating that RF/C-TaSA owns higher contents of quinoid units in the skeleton. The detailed carbon composition of the resins is determined by integrating their ¹³C NMR spectra (Supplementary Fig. 10 and Supplementary Table 2). The ratio of quinoid/benzenoid and percentage of methine linker (-C=) over RF/C-TaSA is 44/56 and 55.7%, respectively, both of which are higher than those of RF (22/78 and 20.1%). The electron acceptors, quinoid units (A), are π -conjugated with inherent electron donors, benzenoid units (D), via methine linker -C=. This optimal π -stacking interaction of D-C=A structure leads to a lower bandgap of RF/C-TaSA and improved carrier transfer efficiency, which extends the light absorption range and improves the separation efficiency of charge carrier (Supplementary Fig. 11)¹⁵.

The light absorption property and electronic structure of as-made materials were revealed by the diffuse reflectance UV-vis spectra and Mott-Schottky measurements. Both RF/C-TaSA and RF/C (anchoring carbon matrix onto RF supports) exhibit stronger absorption than RF (Fig. 2a), attributed to the charge transfer transition of the D-C=A couples. This implies a higher number of quinoid units in RF/C-TaSA and RF/C than that in RF¹⁵. The energy band gap (E_g) of RF/C-TaSA, RF/C and RF is determined to be 1.33 eV, 1.28 eV and 1.95 eV, respectively, through the Tauc plots from Kubelka-Munk function transformation (Fig. 2a, inset and Supplementary Fig. 12). Furthermore, the conduction band edge potential (E_{CB}) of RF/C-TaSA, RF/C and RF was determined to be -0.59 V, -0.60 V and -0.69 V (*vs* SHE at pH = 0) according to the Mott-Schottky plots results, respectively, which are more negative than the redox potential (-0.33 V) of O₂/O₂⁻ pair. These results indicate that the oxygen reduction reaction (ORR) on the above samples is thermodynamically feasible (Fig. 2b). The straight lines with positive slopes in Supplementary Fig. 12 of as-prepared samples confirm their n-type feature, indicating that electron is the majority carrier¹⁶. Furthermore, RF/C-TaSA can generate more electrons with a higher concentration ($5.60 \times 10^{19} \text{ cm}^{-3}$) than RF/C ($3.46 \times 10^{19} \text{ cm}^{-3}$) and RF ($3.33 \times 10^{19} \text{ cm}^{-3}$) (Supplementary Note 1)¹⁷.

The charge carrier generation, mobility and electrical conductivity changes of different photocatalysts were revealed by

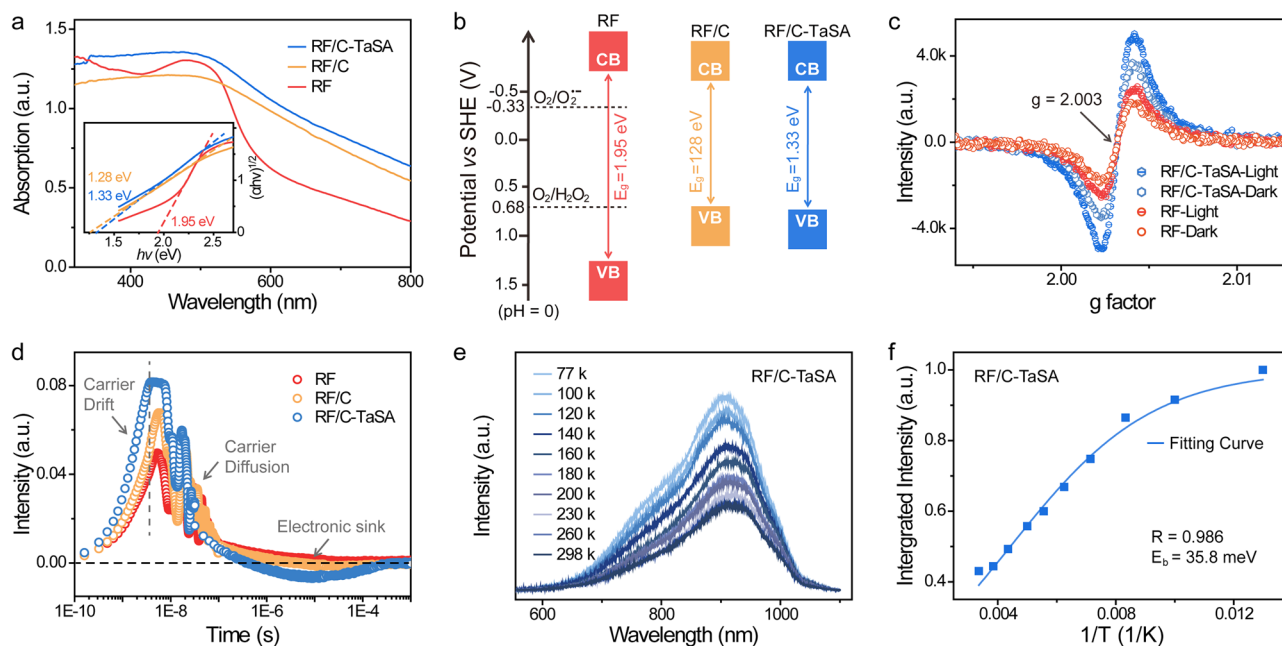


Fig. 2 | Optical, excitation properties and carrier mobility of RF/C-TaSA, RF/C and RF. a UV-Vis spectra of RF/C-TaSA and RF. The inset shows the corresponding Tauc-plot of the $(\alpha h\nu)^{1/2}$ versus $h\nu$. **b** Energy band diagrams of RF/C-TaSA, RF/C and RF. **c** EPR spectra of RF/C-TaSA and RF. **d** Transient photovoltage (TPV) of TAPT-PD-

ST excited at 355 nm. **e** Temperature-dependent photoluminescence spectra excited at 365 nm and **f** integrated photoluminescence intensity as a function of the temperature of RF/C-TaSA. Source data are provided as a Source Data file.

electron paramagnetic resonance (EPR), photocurrent measurement, electrochemical impedance (EIS) and steady-state photoluminescence emission spectroscopy (PL) measurement. A Lorentzian line, corresponding to the π -electrons ($g = 2.003$), is observed in the EPR spectra of RF/C-TaSA, RF/C and RF (Fig. 2c and Supplementary Fig. 13)¹⁸. Upon visible light irradiation, RF/C-TaSA exhibits a stronger EPR signal and higher photocurrent density (Supplementary Fig. 14) than RF/C or RF, indicating that RF/C-TaSA has an enhanced π -electron delocalization and the stronger ability for producing the unpaired photogenerated electrons at its conduction band than RF/C and RF¹⁹. RF/C-TaSA exhibits smaller charge transfer resistance and emission intensity than RF/C or RF (Supplementary Figs. 15–16), implying the reduced transmission resistance from the bulk to the surface-active site and the retarded radiative recombination of charge carrier.

The unique role of the carbon matrix and Ta single-atom sites in enhancing charge separation efficiency was investigated through transient photovoltage (TPV, nanosecond to microsecond timescale) and temperature-dependent photoluminescence measurements. TPV profiles reveal two distinct charge dynamics: (1) All samples exhibit positive carrier drift signals (10^{-10} – 10^{-7} s), confirming hole accumulation at surfaces as a universal feature. Notably, RF/C-TaSA achieves the fastest signal saturation, providing direct evidence of enhanced exciton dissociation due to single-atom incorporation. (2) RF/C-TaSA displays negative diffusion signals in the 10^{-6} – 10^{-4} s range, indicating that photogenerated charges from exciton dissociation are trapped within the carbon matrix²⁰ (Fig. 2d). These results demonstrate that the carbon matrix acts as an effective electron reservoir, temporarily stabilizing photogenerated electrons. This charge-buffering mechanism suppresses electron-hole recombination, significantly boosting photocatalytic performance. Furthermore, temperature-dependent photoluminescence measurements reveal a reduced exciton binding energy in the Ta single-atom-anchored photocatalyst. The integrated

photoluminescence intensity decreases with increasing temperature (Fig. 2e). The exciton binding energy (E_b) of RF/C-TaSA obtained from the fitting based on the Arrhenius equation [$I(T) = I_0/(1 + \text{Aexp}(-E_b/k_B T))$] is 35.8 meV (Fig. 2f), much lower than those of RF/C (52.4 meV) (Supplementary Fig. 17) and RF (50.8 meV) (Supplementary Fig. 18), indicating a less energy loss occurring in the exciton dissociation²¹.

Efficient H₂O₂ and value-added chemicals photosynthesis

The photosynthesis of H₂O₂ and value-added chemicals over RF/C-TaSA was evaluated using benzyl alcohol as the biomass derivative under visible-light irradiation. The yield of benzaldehyde was determined by an internal standard method by using dodecane as the standard substance (Supplementary Fig. 19). The yield of H₂O₂ was determined by the iodometry method, colorimetric method with TMB/H₂O₂/HRP reaction and Ce⁴⁺ titration method (Supplementary Figs. 20–23). The effect of Ta loading content on the RF for the synthesis of H₂O₂ and benzaldehyde (Supplementary Figs. 24–25) reveal that RF/C-TaSA shows a significantly enhanced H₂O₂ production rate of 5.05 mmol/(L h) and benzaldehyde, which is also 2.1 and 3.4 folds higher than that of RF/C and RF, respectively (Fig. 3a). RF/C-TaSA owns a similar specific surface area with RF/C and lower specific surface areas than RF, suggesting the performance improvement originates from higher intrinsic activity of RF/C-TaSA (Supplementary Fig. 26). Moreover, RF/C-TaSA has a larger water contact angle (37.2°) than RF (19.0°) (Supplementary Fig. 27), enabling RF/C-TaSA with the higher dispersion in organic phase than aqueous phase (Supplementary Fig. 28). The solid-organic-aqueous three-phase system is conducive to a spontaneous separation of as-produced H₂O₂ from the biomass derivatives, thus avoiding further energy-consuming separation procedures. This photosynthetic system design can also inhibit the undesirable decomposition of H₂O₂ over the photocatalyst surface by driving as-produced H₂O₂ away from the organic phase where

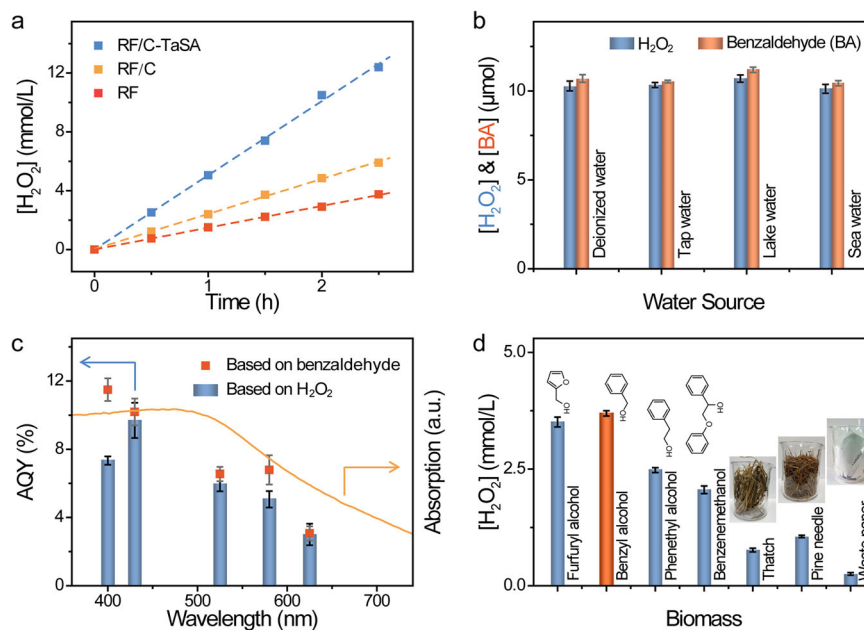


Fig. 3 | Solar-driven H₂O₂ production and biomass-upgraded chemicals over different catalysts. a Time profiles of H₂O₂ photosynthesis by various RF photocatalysts. Experimental conditions: Toluene (2 mL), benzyl alcohol (0.5 mL), water (2 mL), photocatalyst (1 g/L), visible-light irradiation ($\lambda \geq 420$ nm, 100 mW/cm²), 1 atm, O₂ and T = 303 K. **b** The yield of H₂O₂ and benzaldehyde comparison over RF/C-TaSA in deionized water, tap water, lake water and seawater. Experimental conditions: photocatalyst (1 g/L) with toluene (2 mL), benzyl alcohol (0.5 mL) and various water sources (2 mL) under visible-light irradiation ($\lambda \geq 420$ nm, 100 mW/cm²) for 1 h and T = 25 °C. **c** Apparent quantum yield (AQY) of RF/C-TaSA as a

function of wavelength (purple 400 nm, blue 430 nm, green 519 nm, yellow 580 nm and red 625 nm). Experimental conditions: photocatalyst (1 g/L) with toluene (2 mL), benzyl alcohol (0.5 mL) and various water sources (2 mL) under 1 h light irradiation and T = 25 °C. **d** The performance of H₂O₂ photosynthesis over RF/C-TaSA by using furfuryl alcohol, benzyl alcohol, phenethyl alcohol and 2-phenoxy-1-phenylethanol (0.5 M) in toluene (2 mL)/water (2 mL) mixed solution or 100 mg of thatch, pine needle, and waste paper powders in water (50 mL) as a proton source. Error bars in **b–d** represent the average values (mean \pm s.d., $n = 3$). Source data are provided as a Source Data file.

photocatalyst locates. As a result, RF/C-TaSA shows a much lower decomposition rate of H_2O_2 than RF due to its hydrophobic properties (Supplementary Figs. 29–30).

The dissolving ions and organics in real waters were previously reported to deactivate the catalyst^{20,22}. However, herein we find that the photosynthetic system design can inhibit the undesirable deactivation of the catalyst by the fact that RF/C-TaSA can achieve efficient photosynthesis of H_2O_2 and benzaldehyde in tap water, lake water, and seawater (Fig. 3b and Supplementary Table 3) almost without the effects from dissolving ions and organics (Supplementary Figs. 31–33 and Supplementary Table 4). Particularly, RF/C-TaSA can fully harvest the most visible light and show good performance for concurrent photosynthesis of H_2O_2 and benzaldehyde even at red light irradiation (635 nm) with a competitive apparent quantum yield of 3.0%. Due to the metastability of H_2O_2 under purple light irradiation, the apparent quantum yields (AQY) of RF/C-TaSA for benzaldehyde photosynthesis is 11.5%, higher than for H_2O_2 photosynthesis 7.3% at 400 nm (Fig. 3c and Supplementary Table 5).

RF/C-TaSA is demonstrated to be quite effective for the photosynthesis of H_2O_2 coupled with selective photocatalytic conversion of biomass derivatives (furfuryl alcohol, benzyl alcohol, phenethyl alcohol and 2-phenoxy-1-phenylethanol, toluene solution, respectively) to value-added chemicals (furfural, benzaldehyde, phenylacetaldehyde and 2-phenoxy-1-phenylethanol, Supplementary Figs. 34–37 and Supplementary Table 6) under the visible light irradiation (Fig. 3d). RF/C-TaSA can achieve efficient photosynthesis of H_2O_2 from the dehydrogenation of more available thatch, pine needles and wastepaper (Supplementary Fig. 38), which were pretreated by soaking the above raw material in alkali liquor to generate soluble products containing alcoholic hydroxyl group²³ (pretreatment is usually inevitable, and can significantly improve biomass conversion efficiency), and shows good chemical stability during four cycle tests (Supplementary Fig. 39).

These results indicate the universality of RF/C-TaSA in devise application scenarios.

Mechanism investigation

To unravel the promotive factors of RF/C-TaSA, the mechanisms of oxygen reduction to H_2O_2 and concurrent oxidation of benzyl alcohol to benzaldehyde were investigated via in-situ FT-IR, along with a series of control experiments with electron and radical scavengers and in-situ electron paramagnetic resonance (EPR). The in-situ FT-IR spectroscopy was used to unveil the reaction intermediate species during the photocatalytic reaction (Fig. 4a). The signals at 890 cm^{-1} and 1090 cm^{-1} , attributed to the stretching vibration bands of oxygen-active species, as well as the signal at 1713 cm^{-1} , ascribed to the stretching vibration band of the aldehyde group, were observed, indicating the occurrence of benzyl alcohol dehydrogenation during the photocatalytic process. The involvement of electrons and superoxide radicals ($\cdot\text{O}_2^-$) in the reaction was revealed by the fact that the addition of AgNO_3 (electron capturer) or benzoquinone ($\cdot\text{O}_2^-$ quencher) can largely suppress the reaction (Supplementary Fig. 40). The quantitative analysis results of H_2O_2 and benzaldehyde photosynthesis by various photocatalysts reveal that the ratio of produced H_2O_2 to benzaldehyde over RF/C-TaSA is -1:1 (Supplementary Fig. 41), being consistent with the atomic ecoefficiency by following the reaction of $\text{O}_2 + \text{C}_7\text{H}_8\text{O}$ (benzyl alcohol) $\rightarrow \text{H}_2\text{O}_2 + \text{C}_7\text{H}_6\text{O}$ (benzaldehyde). These results support that the hydrogen source of H_2O_2 originates from the dehydrogenation of benzyl alcohol rather than the reported $\cdot\text{O}_2^-$ disproportionation.

In-situ EPR results with 5,5-dimethyl-1-pyrroline N-oxide (DMPO) as spin trapping agent reveal that RF/C-TaSA possesses an enhanced $\cdot\text{O}_2^-$ and $\cdot\text{OOH}^-$ radical response relative to RF (Fig. 4b). By further combining with the quantitative results, we propose herein that the $\cdot\text{OOH}^-$ radical was formed *via* the protonation of $\cdot\text{O}_2^-$, with the benzyl alcohol

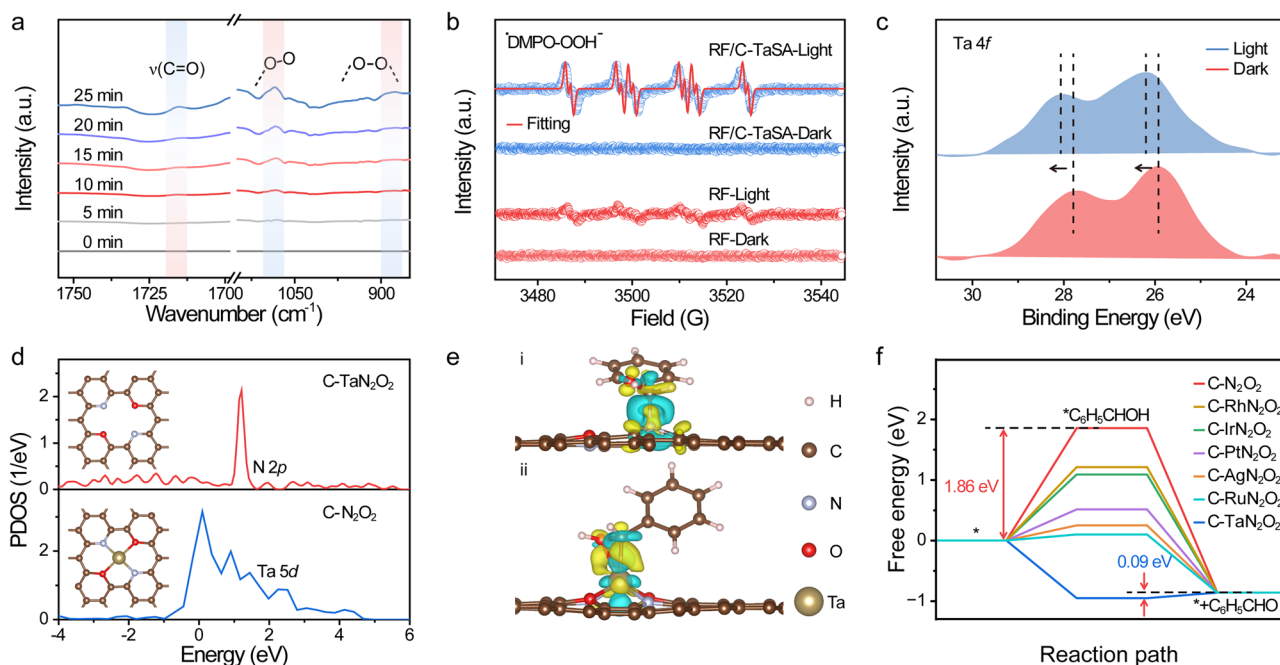


Fig. 4 | Mechanism of H_2O_2 and high value-added benzaldehyde photosynthesis of RF/C-TaSA and RF. **a** In situ FTIR spectrum analysis of photocatalytic H_2O_2 and benzaldehyde production over RF/C-TaSA. **b** In situ EPR spectra of oxygen active species over RF/C-TaSA and RF. The room-temperature EPR spectra were measured after in situ illumination for 5 min by using 5,5-dimethyl-1-pyrroline N-oxide (DMPO) as a trapping agent in pure benzyl alcohol. **c** The in-situ irradiated Ta 4f XPS was measured under light irradiation and in darkness. **d** Projected density of

states (PDOS) of $\text{C-N}_2\text{O}_2$ and $\text{C-TaN}_2\text{O}_2$. **e** Charge density mapping between $\cdot\text{C}_6\text{H}_5\text{CHOH}$ group and catalysts: (i) $\text{C-N}_2\text{O}_2$ and (ii) $\text{C-TaN}_2\text{O}_2$. The iso-surface of charge density is set to $0.005\text{ e}^- \text{ \AA}^{-3}$. The sky-blue and yellow isosurfaces stand for the negative and positive charges, respectively. The dashed lines stand for the Fermi level. **f** Calculated energy profile of benzyl alcohol oxidation into benzaldehyde at $U = 0\text{ V}$ vs. SHE at $\text{pH} = 7$. Source data are provided as a Source Data file.

deprotonated reaction providing the proton²⁴. Rotating disk electrode (RDE) results reveal the average electron transfer number (n) of ORR on RF/C-TaSA is close to 2, supportive of the 2-electron-transfer pathway (Supplementary Fig. 42). Additionally, open-circuit-potential measurements show that RF/C-TaSA has a reduced width of the depletion region (w_d) of 3.3 nm, compared to those of than RF/C (4.3 nm) and RF (4.5 nm) (Supplementary Fig. 43 and Supplementary Note 2). The smallest w_d of RF/C-TaSA possesses a wide conduction region, favoring carriers transfer from catalyst to adsorbed substrates¹⁷.

The oxidation and reduction active sites, along with the enhanced photocatalytic performance of the RF/C-TaSA, were investigated through in-situ XPS and DFT calculations. In-situ irradiated XPS analysis was employed to identify the oxidative and reductive sites on RF/C-TaSA. Under light irradiation, the binding energies of Ta 4*f* and O 2*p* exhibit a notable positive shift relative to the dark control (Fig. 4c), strongly indicating the accumulation of photogenerated holes at Ta and O sites. Conversely, the binding energies of C 2*p* and N 2*p* shift negatively, suggesting electron accumulation at C and N sites (Supplementary Fig. 44 and Supplementary Table 7). These results demonstrate that the phenolic resin absorbs visible light, generating exciton pairs that preferentially migrate into the carbon matrix due to its conjugated π -electron delocalization. The tantalum single atoms anchored on the carbon matrix further promote exciton dissociation, with holes localized at Ta sites and electrons stabilized within the carbon matrix's electron reservoir. This synergistic mechanism—combining efficient light absorption, exciton migration, and charge separation—explains the superior photocatalytic performance of RF/C-TaSA relative to RF/C and RF (Supplementary Fig. 45).

This observation implies TaSA to be the main oxidation site in RF/C-TaSA during photosynthesis, further demonstrated by the calculated projected density of states (PDOS) (DFT calculation structures are provided as Supplementary Data 1). As shown in Fig. 4d, the Ta 5*d*

states are mainly distributed in the region centered around the Fermi level, which enables TaSA with optimized electronic properties for bonding with the dehydrogenation intermediate of benzyl alcohol. The surface catalytic reaction was further studied by presenting energy profiles of benzyl alcohol oxidation into benzaldehyde. The result shows that the TaSA can greatly enhance the dehydrogenation of benzyl alcohol by forming two chemical bonds (C-Ta and O-Ta) between TaSA and *C_6H_5CHOH intermediate. However, only one N-C bond forms between C-N₂O₂ and *C_6H_5CHOH intermediate in the absence of TaSA. Such strong interaction between catalyst and intermediate was also demonstrated by the charge density mapping, showing the obvious electron transfer from *C_6H_5CHOH intermediate to TaSA through the formed dual chemical bonds (Fig. 4e). Moreover, the TaN₂O₂ site also shows a higher alcohol dehydrogenation performance than the common noble metal thermal catalysts (Ag, Ir, Pt, Rh and Ru) (Fig. 4f). This novel TaN₂O₂ active site can avoid the photo-corrosion issues observed in sulfide and nitride photocatalysts and extend the lifetime of the photocatalyst.

To test the practicability and long-term stability of concurrent photosynthesis of H₂O₂ and value-added benzaldehyde of our RF/C-TaSA, a solar-powered device was designed (Fig. 5a, Supplementary Fig. 46 and Supplementary Movie 1). We found that RF/C-TaSA did not show obvious activity decay even after 70 days (from July 23rd, 2022 to October 15th, 2022; 8 h sunlight irradiation for each day) of consecutive cycles (Fig. 5b, Supplementary Figs. 47–51 and Supplementary Table 8) according to TEM (Supplementary Fig. 52) and XANES results (Supplementary Fig. 53). H₂O₂ products with high concentrations can avert the extra energy-consuming concentration procedure. The device can automatically extract H₂O₂ from the organic phase to aqueous phase in a gas-liquid-liquid dispersion system, resulting in a hundred milliliter H₂O₂ product with high concentration (64.5 mmol/L) (Fig. 5b, this data was collected in September 1st, 2022). The concentration of the

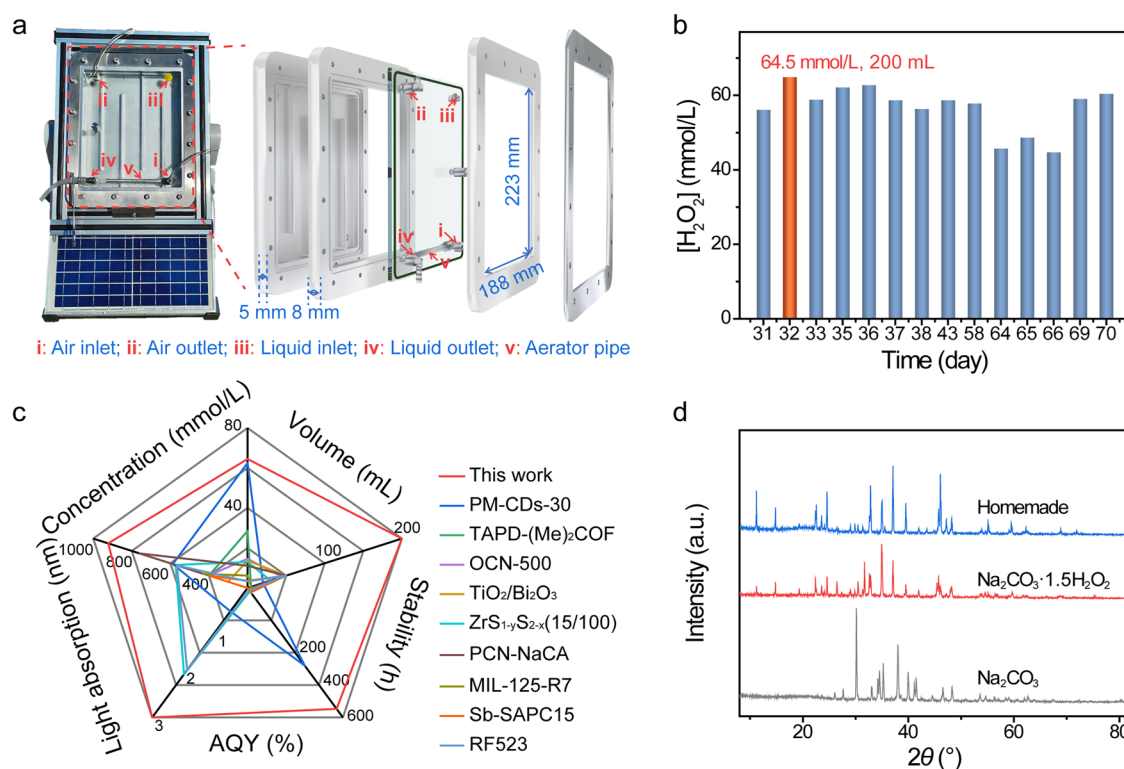


Fig. 5 | Performance of homemade solar-powered device. **a** Schematics of self-designed homemade micro-reactor. **b** Cyclic stability of RF/C-TaSA catalyst tested by a solar-powered micro-reactor. Experimental conditions: benzyl alcohol (150 mL), water (200 mL), photocatalyst (2 g/L), natural light irradiation and

outdoor (40.02° N and 116.32° E). **c** Comprehensive comparison of catalytic performance between RF/C-TaSA and reported state-of-the-art photocatalysts. **d** X-ray diffraction (XRD) patterns of the Na₂CO₃, Na₂CO₃·1.5H₂O₂, and homemade Na₂CO₃·1.5H₂O₂. Source data are provided as a Source Data file.

hydrogen peroxide product reached the commercial grade (*c.a.*, 876 mmol/L) (Supplementary Fig. 54). As a result, the present solar-powered device can gain \$262.35 (USD) *per* one-kilogram H₂O₂ (Supplementary Note 3). Moreover, the concentration of the H₂O₂ product, the AQY value, the stability and light absorption property of our sample are competitive with those of other reported photocatalysts (Fig. 5c and Supplementary Table 5)^{12,15,20,25–30}. Additionally, the crude and concentrated H₂O₂ can be used to produce solid H₂O₂ powder (Na₂CO₃ · 1.5H₂O₂), as confirmed by XRD (Fig. 5d, detailed preparation process was given in Supplementary Information). The solid H₂O₂ powder products are more reliable and easier for storage than the liquid H₂O₂³¹. The Na₂CO₃ · 1.5H₂O₂ powders maintain high sterilization activities after 6 months (Supplementary Fig. 55).

Discussion

We report a composite RF/C-TaSA photocatalyst with TaN₂O₂ atomic sites with more visible light adsorption property for efficient separation-free photosynthesis of H₂O₂ and biomass-upgraded chemicals with industrially-relevant performance from oxygen and biomass. Solid-state ¹³C NMR, FTIR, and UV–vis spectra reveal that RF/C-TaSA with an optimal benzenoid-quinoid donor-acceptor (D-A) structure has a low band gap and maximized visible light harvesting. DFT simulations and experimental results verify TaSA to be the active site for the dehydrogenation of biomass or its derivatives. RF/C-TaSA photocatalyst can utilize more visible light and achieve a competitive apparent quantum yield of 3.0% at 635 nm for the simultaneous photosynthesis of H₂O₂ and biomass-upgraded chemicals. More practically, RF/C-TaSA photocatalyst can produce H₂O₂ by the use of thatch, pine needle, and wastepaper as a proton source. The RF/C-TaSA photocatalyst delivers good durability over a consecutive 70-day photocatalytic operation in a homemade micro-reactor. We directly obtained a concentrated H₂O₂ solution of commercial-grade 3 wt%, avoiding further energy-intensive separation. The crude concentrated H₂O₂ can be readily converted to solid H₂O₂ powder (Na₂CO₃ · 1.5H₂O₂) for ease of storage and transport.

Methods

Materials

Tantalum Chloride (TaCl₅) was purchased from Meryer Technologies Co., Ltd. Urea, citric acid and ammonium hydroxide were purchased from Aladdin Reagent Co., Ltd. The resorcinol was purchased from Macklin Co., Ltd. Formaldehyde and tetraethyl silicate (TEOS) were obtained from Xilong Scientific Co., Ltd. All chemicals were used as received without further purification.

Synthesis of resorcinol–formaldehyde resins with yolk-shell structure (RF)

RF was synthesized according to a reported recipe with minor modifications.¹ In a typical synthesis, resorcinol (0.15 g) and formaldehyde (37 wt%, 0.21 mL) were added to a mixture containing ammonia aqueous solution (28 wt%, 3.0 mL), deionized water (10 mL) and ethanol (70 mL). The mixture was then vigorously stirred for 4 h at 25 °C, followed by the addition of 0.6 mL TEOS. After the mixture was further stirred for 30 mins, 0.4 g resorcinol and 0.56 mL formaldehyde (37 wt %) were added. Then, the mixture was stirred for another 2.5 h at 25 °C. The resulting product was collected by centrifugation and then dispersed in deionized water (30 mL), and left in an autoclave under hydrothermal conditions at 453 K for 18 h. The as-obtained product was etched using 4 M NH₄HF₂ solvent for 72 h to remove the silica completely, washed with deionized water and acetone three times and dried under ambient conditions. The yellow product was ground thoroughly before characterization.

Synthesis of RF/C

100 mg of RF was dispersed in 200 μL of C-TaN₂O₂ aqueous solution with a concentration of 50 g/L (1.0 wt%). After 6 h, the RF/C was made

by freeze-drying and subsequent calcining in Ar at 220 °C for 2 h. The yield of the corresponding photocatalyst is 80.0%.

Synthesis of carbon matrix (C-N₂O₂)

In a typical synthesis, 12 mmol of urea and 2 mmol of citric acid were dissolved in a 60 mL aqueous solution. The mixture was transferred into a Teflon-lined stainless-steel autoclave and thermally treated under 180 °C for 2–18 h. The produced C-N₂O₂ sample was centrifuged at 9500 rpm/min for 5 min to discard the deposits, and then was on dialysis for 1 day (MWCO, 3500). After freeze-drying, the C-N₂O₂ was obtained as a black powder.

Synthesis of C-(TaSA)_x (x = 0.5, 1, 2, TaSA = TaN₂O₂)

Ta single atom anchored on carbon matrix [C-(TaSA)_x] was synthesized similar to that of C-N₂O₂ except the addition of TaCl₅ with different dosages [7.2 mg, 14.4 mg, and 28.8 mg, for C-(TaSA)_{0.5}, C-(TaSA)₁ (abbreviated as C-TaSA, alternative name as C-TaN₂O₂, the yield of the corresponding photocatalyst is 7.0%) and C-(TaSA)₂, respectively] in 60 mL aqueous solution.

Synthesis of RF/(C-TaSA)_x (x = 0.5, 1, 2)

100 mg of RF was dispersed in 200 μL of C-TaSA aqueous solution with different concentrations [25 g/L, 50 g/L, 100 g/L, for RF/(C-TaSA)_{0.5} (0.5 wt%), RF/(C-TaSA)₁ (1.0 wt%), and RF/(C-TaSA)₂ (2.0 wt%), respectively]. After anchoring for 6 h, RF/(C-TaSA)_x was collected by freeze-drying and subsequent calcining in Ar at 220 °C for 2 h. The yield of the corresponding photocatalyst is 93.0%. RF/(C-TaSA)₁ with the best catalytic performance was referred to as RF/C-TaSA.

Synthesis of solid H₂O₂ product (Na₂CO₃ · 1.5H₂O₂)

The solid H₂O₂ was prepared by recrystallization method. Typically, the crude hydrogen peroxide product (10 mL) generated by the device was slowly added into the mixed solution containing 10 mL saturated sodium carbonate (29.4 g/L at 25 °C) and 15 mL isopropanol-triethanolamine (volume ratio of 3:1). Notably, a mixture of 0.1 g Na₂SO₃ and MgCl₂ in a ratio of 3:1 was added into the isopropanol-triethanolamine mixed solution as the stabilizer for solid H₂O₂. During the recrystallization process, the temperature of the reaction solution needs to be maintained at 15 °C. After stirring the mixed solution for 30 minutes, the solution was undisturbed for crystallization. The obtained recrystallized product was washed twice with ethyl alcohol. Finally, the white powder was dried at a temperature of 60 °C prior to further measurement.

Catalytic evaluation

The photocatalytic synthesis of H₂O₂ and benzaldehyde from benzyl alcohol was carried out under an O₂ atmosphere (1 atm) in a 25 mL round-bottomed Pyrex glass flask with a sealed spigot. The suspension was prepared by mixing benzyl alcohol (2 mL), deionized water (2 mL) and catalyst (0.5 g/L) in a reactor equipped with a stir bar. The reactor was irradiated using a white LED light (0–200 mW/cm²) whilst stirring at 20–50 °C. The H₂O₂ generated in the reaction was determined by a typical iodometry method, and the yield of benzaldehyde was determined by gas chromatography described in Supplementary Information. The H₂O₂ product obtained from a small reaction system (2 mL benzyl alcohol and 2 mL water) was first centrifuged at 7500 rpm for 5 min and then filtrated by the needle-type filter (0.22 μm) for further quantification. The crude H₂O₂ products obtained from solar-powered devices (150 mL benzyl alcohol and 200 mL water) were filtrated by Reverse Osmosis (RO) to eliminate the potential impact of soluble organic matter on the detection. It should be noted that only typical substrates are selected for qualitative analysis due to the complex components in aqueous solution (Supplementary Fig. 56). After the reaction, the gluconolactone and furfural fragment were detected by liquid mass spectrometry (Supplementary Figs. 57, 58).

Structural characterization

XAFS spectra at the Ta L₃-edge were measured at the 1WB beamline of the Beijing Synchrotron Radiation Facility (BSRF) and the BL20U1 beamline of the Shanghai Synchrotron Radiation Facility (SSRF). The obtained XAFS data were processed in Athena (version 0.9.26) for background, pre-edge line and post-edge line calibrations. Then, the Fourier transformed fitting was carried out in Artemis (version 0.9.26). The k³ weighting, k-range of 3–12 Å⁻¹ and R range of 1–3.6 Å were used for the fitting of Ta foil; k-range of 3–11 Å⁻¹ and R range of 1–3 Å were used for the fitting of Ta. The four parameters, coordination number, bond length, Debye-Waller factor and E0 shift (CN, R, σ², ΔE₀) were fitted without anyone being fixed, constrained, or correlated. For Wavelet Transform analysis, the χ(k) exported from Athena was imported into the Hama Fortran code. The parameters were listed as follows: R range, 1–4 Å, k range, 0–13 Å⁻¹ for Ta foil and 0–11 Å⁻¹ for Ta sample; k weight, 2; and Morlet function with κ=10, σ=1 was used as the mother wavelet to provide the overall distribution. Aberration-corrected high-angle annular dark-field scanning transmission electron microscopy (HAADF-STEM) was conducted on the JEMARM200F transmission electron microscope with an accelerating voltage of 300 kV. The samples were characterized on a powder X-ray diffractometer (Rigaku D/max2400) equipped with a Cu Kα radiation source (λ = 1.5418 Å). The morphology of different samples was characterized using transmission electron microscopy (TEM, Tecnai G2 F20 S-Twin) and scanning electron microscopy (SEM, Hitachi S4800). The surface area of different samples was determined on a TriStar-3020 using the Brunauer–Emmett–Teller (BET) method. X-ray photoelectron spectroscopy (XPS) and in situ XPS data were obtained on a USA Thermo ESCALAB 250 with a monochromatized Al Kα line source (200 W). The spectra deconvolution was carried out by XPS PEAK41 software packages. The in situ FTIR spectra measurements were performed on a Bruker Tensor FTIR spectrometer equipped with an MCT detector. Steady-state photoluminescence (PL) spectra were recorded on an LP980 fluorescence lifetime spectrophotometer under the excitation of 365 nm and probed at 460 nm. The UV–Vis diffuse reflectance spectra (DRS) were obtained on a Shimadzu UV–3600 UV–Vis–NIR spectrophotometer using BaSO₄ as a reference and the diffuse reflectance accessory. The electron paramagnetic resonance (EPR) measurements were obtained using a Bruker model EMXPLUS 10/12 spectrometer. The solid-state Nuclear Magnetic Resonance was carried out on Bruker-600M Hz NMR.

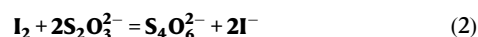
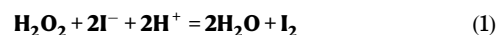
DFT calculations

The oxidation of benzyl alcohol into benzaldehyde was investigated on C-TaN₂O₂ by the Vienna Ab-initio Simulation Package (VASP) with the revised Perdew–Burke–Ernzerhof (RPBE) of the generalized gradient approximation (GGA). The interaction between ionic and valence electrons was simulated by PAW pseudo-potential. A 4 × 3 carbon supercell was used to support the TaSA. The experimentally confirmed Ta-N₂O₂ structure was built in the carbon supercell. The geometry optimization adopted the cutoff energy of 450 eV and energy convergence of 1 × 10⁻⁴ eV at the gamma point. After geometry optimization, the projected density of state (PDOS) and charge density mappings were calculated with energy convergence of 1 × 10⁻⁵ eV, Monkhorst-Pack k-point mesh of 2 × 2 × 1, and the cutoff energy of 450 eV. The calculations of Gibbs free energy changes (ΔG) of all reaction steps adopted the known standard hydrogen electrode (SHE) model at U = 0 V vs. SHE at pH = 7³².

Quantification methods

Iodometry method. The H₂O₂ generated in the reaction was determined by a typical iodometry method. Typically, 1 mL of the reaction

solution was filtered after illumination for 1 h, and then 10 μL of sulfuric acid solution (1 mL sulfuric acid was mixed with 8 mL deionized water) was dropped into the above filtrate. After that, 1 g of KI and 30 μL of ammonium molybdate (30 g/L) were added. The resultant mixture was allowed to equilibrate with magnetic stirring for 5 min. Finally, the mixture was titrated using a mixture solution of Na₂S₂O₃ and Na₂CO₃ (2.5 g/L of Na₂S₂O₃·5H₂O, 0.02 g/L of Na₂CO₃) until the solution became colorless. In the controlled reaction, water was used as the contrast. The reactions between H₂O₂, I₂ and Na₂S₂O₃ were shown below.



Colorimetric method with TMB/H₂O₂/HRP reaction. 50 μL of H₂O₂ with various concentrations of 0–0.15 mM were mixed with 425 μL of phosphate-buffered saline (PBS) solutions (pH = 7.4) containing 17.6 mM TMB and 25 μL of 1 μg/mL horseradish peroxidase (HRP) PBS solutions. After standing for 5 min, the reaction was terminated by adding 500 μL of 0.3 M sulfuric acid solution. Finally, the absorption values of resultant solutions were measured at 450 nm. All experiments were performed in triplicate. Based on the quantitative steps above, the linear calibration curve was obtained.

Ce⁴⁺ titration method. The H₂O₂ concentration was measured by the cerium sulfate titration method based on the stoichiometry of 2Ce⁴⁺ + H₂O₂ = 2Ce³⁺ + 2H⁺ + O₂. In atypical operation, 10 μL of H₂O₂ with various concentrations (0–0.4 mM, **Note:** High concentrations of hydrogen peroxide should be diluted) was added into a certain amount of Ce⁴⁺ solution to reduce Ce⁴⁺ to Ce³⁺. The Ce⁴⁺ concentration can be detected by spectrophotometry at 316 nm. Thus, we calculated H₂O₂ concentration via the equation as follows:

$$C(\text{H}_2\text{O}_2) = \frac{[C_0(\text{Ce}^{4+}) - C(\text{Ce}^{4+})] \times V(\text{Ce}^{4+})}{2 \times V(\text{H}_2\text{O}_2)} \quad (3)$$

GC methods. The internal standard method of using dodecane as a standard substance was used to quantify the content of benzaldehyde. The analysis of benzaldehyde was conducted in a Gas chromatography (GC, Agilent 7890B) equipped with a 30 m DB-WAX UI capillary column (0.32 mm) and a flame ionizing detector. The temperature at the injector port and detector was set at 210 and 240 °C, respectively. For better separation and analysis of the product, the initial temperature of oven was set at 80 °C. After maintained at 80 °C for 3 min, the temperature of the oven increased to 170 °C at the rate of 20 °C/min and maintained at 170 °C for 3 min. Finally, the temperature of the oven was further improved to 200 °C at the rate of 20 °C/min and maintained for 3 min. The retention time for dodecane, benzaldehyde and benzyl alcohol are 5.2 min, 8.1 min and 11.5 min, respectively. The relative correction factor between benzaldehyde and dodecane obtained from the standard curve is 0.607, indicating that the molarity of benzaldehyde (C_{BD}) can be calculated by the following formula:

$$C_{\text{BD}} = 0.607 \times C_{\text{Dodecane}} \times (A_{\text{BD}}/A_{\text{Dodecane}}) \quad (4)$$

C_{Dodecane}: Molarity of dodecane; A_{BD}: Peak area of benzaldehyde; A_{Dodecane}: Peak area of dodecane.

After the reaction, 1 mL of 2.5 mM dodecane in toluene solution was added into 1 mL organic phase products. 2 μL liquid was taken from above mixed solution for chromatographic detection.

Photoelectrochemical measurements

The working electrode was prepared by the drop-casting method. In a typical process, 2 mg of the catalyst powder was mixed with 0.3 mL of

isopropyl alcohol, 0.7 mL of H₂O and 10 μL of naphthol mixed solution by sonication. Then, 20 μL of the slurry was dropped onto a fluorine-doped tin oxide (FTO, 2 × 1.5 cm) glass electrode through a layer-by-layer method. Photocurrent measurements were performed under LED light illumination conditions in a 0.2 M Na₂SO₄ solution (pH: 6.6) by using the i-t technique. Mott–Schottky plots were also obtained with the working electrodes immersed into 0.2 M Na₂SO₄ aqueous solution by using the impedance–potential technique.

The potential conversion relation is according to the Nernst equation:

$$E(\text{NHE}) = E(\text{Ag}/\text{AgCl}) + 0.197V \quad (5)$$

$$E(\text{RHE}) = E(\text{NHE}) + 0.0591 \times \text{pH} \quad (6)$$

Note: The potential of RHE is related to pH value. At the pH of 0, the potential of RHE is equivalent to SHE.

The electrochemical impedance spectra (EIS) were obtained by using the A. C. impedance technique. The working electrode was immersed into a mixture containing 0.1 M KCl, 2 mM K₃[Fe(CN)₆] and 2 mM K₄Fe(CN)₆·3H₂O. All the above tests were conducted on a workstation (CHI760D, CH Instruments, Inc., Shanghai, China) in a three-electrode model, with Pt wire as the counter electrode and Ag/AgCl electrode (saturated KCl) as the reference electrode.

The detailed experimental procedures and reaction conditions for AQY testing are as follows:

The light source here is the LED lamp (purple 400 nm, blue 430 nm, green 519 nm, yellow 580 nm, red 625 nm) and the irradiation area is controlled as 1 × 10⁻⁴ m².

The AQY efficiency was determined using the following equation:

$$\Phi\text{AQY}(\%) = \frac{\text{(the number of H}_2\text{O}_2\text{ molecules} \times 2)}{\text{(photon number)} \times 100\%} \quad (7)$$

The photon number (N) was calculated by the following equation: $N = E\lambda/hc$. Here, λ is the central wavelength of the LED light, h is the Planck constant, c is the speed of light, and E is the energy of the light. Furthermore, the energy of the light was calculated as $E = \text{light intensity (mW/cm}^2) \times \text{irradiated area (cm}^2) \times \text{reaction time (s)}$.

Data availability

None Source data are provided with this paper.

References

- Sun, J. et al. Pyrene-based covalent organic frameworks for photocatalytic hydrogen peroxide production. *Angew. Chem. Int. Ed.* **62**, e202216719 (2023).
- Chen, Y. et al. Hierarchical assembly of donor–acceptor covalent organic frameworks for photosynthesis of hydrogen peroxide from water and air. *Nat. Synth.* **3**, 998–1010 (2024).
- Zhang, X. et al. Keto-anthraquinone covalent organic framework for H₂O₂ photosynthesis with oxygen and alkaline water. *Nat. Commun.* **15**, 2649 (2024).
- Liu, R. et al. Linkage-engineered donor–acceptor covalent organic frameworks for optimal photosynthesis of hydrogen peroxide from water and air. *Nat. Catal.* **7**, 195–206 (2024).
- Huang, Y. et al. Achieving a solar-to-chemical efficiency of 3.6% in ambient conditions by inhibiting interlayer charges transport. *Nat. Commun.* **15**, 5406 (2024).
- Choi, J. Y. et al. Photocatalytic hydrogen peroxide production through functionalized semiconductive metal–organic frameworks. *J. Am. Chem. Soc.* **146**, 11319–11327 (2024).
- Isaka, Y. et al. Photocatalytic production of hydrogen peroxide through selective two-electron reduction of dioxygen utilizing amine-functionalized MIL-125 deposited with nickel oxide nanoparticles. *Chem. Commun.* **54**, 9270–9273 (2018).
- Li, Y., Pei, Z., Luan, D. & Lou, X. W. D. Triple-phase photocatalytic H₂O₂ production on a Janus fiber membrane with asymmetric hydrophobicity. *J. Am. Chem. Soc.* **146**, 3343–3351 (2024).
- Zhang, W., Chao, Y. & Guo, S. Electro-(Photo)catalysis for concurrent evolution of hydrogen and high value-added chemicals. *Energy Lab.* **1**, 220004 (2023).
- Zhai, G. Y. et al. Highly efficient, selective, and stable photocatalytic methane coupling to ethane enabled by lattice oxygen looping. *Sci. Adv.* **10**, eado4390 (2024).
- Inoue, Y. Photocatalytic water splitting by RuO₂-loaded metal oxides and nitrides with d⁰- and d¹⁰-related electronic configurations. *Energy Environ. Sci.* **2**, 364–386 (2009).
- Teng, Z. et al. Atomically dispersed antimony on carbon nitride for the artificial photosynthesis of hydrogen peroxide. *Nat. Catal.* **4**, 374–384 (2021).
- Shiraishi, Y., Matsumoto, M., Ichikawa, S., Tanaka, S. & Hirai, T. Polythiophene-doped resorcinol–formaldehyde resin photocatalysts for solar-to-hydrogen peroxide energy conversion. *J. Am. Chem. Soc.* **143**, 12590–12599 (2021).
- Wang, S., Sun, M., Zheng, L. & Zhou, S. On the promising performance of single Ta atom in efficient nitrogen fixation. *Chem. Catal.* **1**, 1322–1330 (2021).
- Shiraishi, Y. et al. Resorcinol–formaldehyde resins as metal-free semiconductor photocatalysts for solar-to-hydrogen peroxide energy conversion. *Nat. Mater.* **18**, 985–993 (2019).
- Hou, Y. et al. Rigid covalent organic frameworks with thiazole linkage to boost oxygen activation for photocatalytic water purification. *Nat. Commun.* **15**, 7350 (2024).
- Tian, Z. et al. Efficient photocatalytic hydrogen peroxide generation coupled with selective benzylamine oxidation over defective ZrS₃ nanobelts. *Nat. Commun.* **12**, 1–10 (2021).
- Kuroda, S., Noguchi, T. & Ohnishi, T. Electron nuclear double resonance observation of resemath π-electron defect states in undoped poly(paraphenylene vinylene). *Phys. Rev. Lett.* **72**, 286–289 (1994).
- Niu, C.-P., Zhang, C.-R., Liu, X., Liang, R.-P. & Qiu, J.-D. Synthesis of propenone-linked covalent organic frameworks via Claisen–Schmidt reaction for photocatalytic removal of uranium. *Nat. Commun.* **14**, 4420 (2023).
- Wu, Q. et al. A metal-free photocatalyst for highly efficient hydrogen peroxide photoproduction in real seawater. *Nat. Commun.* **12**, 483 (2021).
- Xu, J. et al. Vinylene-linked covalent organic frameworks (COFs) with symmetry-tuned polarity and photocatalytic activity. *Angew. Chem. Int. Ed.* **132**, 24053–24061 (2020).
- Gopakumar, A. et al. Lignin-supported heterogeneous photocatalyst for the direct generation of H₂O₂ from seawater. *J. Am. Chem. Soc.* **144**, 2603–2613 (2022).
- Wakerley, D. W. et al. Solar-driven reforming of lignocellulose to H₂ with a CdS/CdO_x photocatalyst. *Nat. Energy* **2**, 17021 (2017).
- Su, F. et al. mpg-C₃N₄-catalyzed selective oxidation of alcohols using O₂ and visible light. *J. Am. Chem. Soc.* **132**, 16299–16301 (2010).
- Krishnaraj, C. et al. Strongly reducing (Diaryl amino)benzene-based covalent organic framework for metal-free visible light photocatalytic H₂O₂ Generation. *J. Am. Chem. Soc.* **142**, 20107–20116 (2020).
- Wei, Z. et al. Efficient visible-light-driven selective oxygen reduction to hydrogen peroxide by oxygen-enriched graphitic carbon nitride polymers. *Energy Environ. Sci.* **11**, 2581–2589 (2018).
- He, B. et al. Cooperative coupling of H₂O₂ production and organic synthesis over a floatable polystyrene-sphere-supported TiO₂/Bi₂O₃ S-scheme photocatalyst. *Adv. Mater.* **34**, 2203225 (2022).

28. Tian, Z. et al. Efficient photocatalytic hydrogen peroxide generation coupled with selective benzylamine oxidation over defective ZrS₃ nanobelts. *Nat. Commun.* **12**, 2039 (2021).
29. Zhao, Y. et al. Mechanistic analysis of multiple processes controlling solar-driven H₂O₂ synthesis using engineered polymeric carbon nitride. *Nat. Commun.* **12**, 3701–3711 (2021).
30. Isaka, Y., Kawase, Y., Kuwahara, Y., Mori, K. & Yamashita, H. Two-phase system utilizing hydrophobic metal–organic frameworks (MOFs) for photocatalytic synthesis of hydrogen peroxide. *Angew. Chem. Int. Ed.* **131**, 5456–5460 (2019).
31. Xia, C. et al. Confined local oxygen gas promotes electrochemical water oxidation to hydrogen peroxide. *Nat. Catal.* **3**, 125–134 (2020).
32. Nørskov, J. K. et al. Origin of the overpotential for oxygen reduction at a fuel-cell cathode. *J. Phys. Chem. B.* **108**, 17886–17892 (2004).

Acknowledgements

This study was financially supported by the National Key R&D Program of China (No. 2022YFE0128500), National Science Fund for Excellent Youth Foundation (No. 52522213), National Science Fund for Distinguished Young Scholars (No. 52025133), Beijing Natural Science Foundation (Z220020), New Cornerstone Science Foundation through the XPLOER PRIZE, National Natural Science Foundation of China (22309005). The authors thank the National Supercomputer Center in LvLiang of China, and the calculations were performed on TianHe-2. The authors also thank the BL20U1 beamline of the Shanghai Synchrotron Radiation Facility (SSRF) for their assistance with the synchrotron radiation testing.

Author contributions

S.G. conceived the project. H.T. designed the experiment and finished the synthesis and characterization. P.Z. conducted the DFT calculations. Y.G. did the electrochemical measurements. W.C. analyzed the Ta L₃-edge X-ray absorption spectroscopy data. F.L., H.L., X.C., Y.L. and L.Z. conducted data analyses and discussions. H.T., P.Z., H.G., M.L. and S.G. co-wrote the manuscript.

Competing interests

The authors declare no competing interests.

Additional information

Supplementary information The online version contains supplementary material available at <https://doi.org/10.1038/s41467-025-63838-9>.

Correspondence and requests for materials should be addressed to Shaojun Guo.

Peer review information *Nature Communications* thanks Qingzhe Zhang and the other anonymous reviewer(s) for their contribution to the peer review of this work. A peer review file is available.

Reprints and permissions information is available at <http://www.nature.com/reprints>

Publisher's note Springer Nature remains neutral with regard to jurisdictional claims in published maps and institutional affiliations.

Open Access This article is licensed under a Creative Commons Attribution-NonCommercial-NoDerivatives 4.0 International License, which permits any non-commercial use, sharing, distribution and reproduction in any medium or format, as long as you give appropriate credit to the original author(s) and the source, provide a link to the Creative Commons licence, and indicate if you modified the licensed material. You do not have permission under this licence to share adapted material derived from this article or parts of it. The images or other third party material in this article are included in the article's Creative Commons licence, unless indicated otherwise in a credit line to the material. If material is not included in the article's Creative Commons licence and your intended use is not permitted by statutory regulation or exceeds the permitted use, you will need to obtain permission directly from the copyright holder. To view a copy of this licence, visit <http://creativecommons.org/licenses/by-nc-nd/4.0/>.

© The Author(s) 2025